Journal of Materials Chemistry C

High carrier lifetimes in epitaxial germanium-tin/Al(In)As heterostructures with variable tin composition

Journal of Materials Chemistry C

High carrier lifetimes in epitaxial germanium-tin/Al(In)As heterostructures with variable tin composition

Mantu K. Hudait*[a], Steven W. Johnston[b], Michael B. Clavel[a], Shuvodip Bhattacharya[a], Sengunthar Karthikeyan[a], and Rutwik Joshi[a]

Group IV-based germanium-tin ($Ge_{1-y}Sn_y$) compositional materials have recently shown great promise for infrared detection, light emission and ultra-low power transistors. High carrier lifetimes are desirable for enhancing the detection limit and efficiency of photodetectors, low threshold current density in laser, and low tunneling barrier height by lowering defects and dislocations at the heterointerface of source and channel. Here, carrier lifetimes in epitaxial germanium (Ge) and variable tin (Sn) compositional $Ge_{1-y}Sn_y$ materials were experimentally determined on GaAs substrates using the contactless microwave photoconductive decay (μ-PCD) technique at an excitation wavelength of 1500 nm. Sharp (2×2) reflection high energy electron diffraction patterns and low surface roughness were observed from the surface of the $Ge_{0.97}Sn_{0.03}$ epilayer. X-ray rocking curves from $Ge_{0.97}Sn_{0.03}$ and $Ge_{0.94}Sn_{0.06}$ layers, demonstrated pseudomorphic and lattice-matched growth on AlAs and $In_{0.12}Al_{0.88}As$ buffer respectively, further substantiated by reciprocal space maps as well as abrupt heterointerfaces evident from the presence of Pendellösung oscillations. High effective carrier lifetimes of 150 ns to 450 ns were measured for $Ge_{1-y}Sn_y$ epilayers as a function of Sn composition, surface roughness, growth temperature, and layer thickness. The observed increase in carrier lifetime with increasing Ge layer thickness and reducing surface roughness, by incorporating Sn, were explained. The enhancement of carrier lifetime with increasing Sn concentration was achieved by controlling the defects with lattice-matched $Ge_{0.94}Sn_{0.06}/In_{0.12}Al_{0.88}As$ heterointerface or pseudomorphic growth of $Ge_{0.94}Sn_{0.06}$ on GaAs. Therefore, our monolithic integration of variable Sn alloy compositional $Ge_{1-y}Sn_y$ materials with high carrier lifetimes opens avenues to realize electronic and optoelectronic devices.

Introduction

Alloying tin (Sn) with epitaxial germanium (Ge) (*i.e.*, $Ge_{1-y}Sn_y$) during material synthesis offers several advantages, chief among them being that the bandgap of Ge will be converted from an indirect (conduction band minimum located at L-valley) bandgap to a direct bandgap (conduction band minimum at Γ-valley) material, which can enhance absorption as well as improve photodetector response. With the addition of 6-8% Sn alloying, which compensates the 0.13 eV difference between the Ge Γ- and L-valleys due to a more rapid decrease in the conduction band minimum of the

former,[1-18] similar to ~1.6% tensile strain in epitaxial Ge.[19-21] The $Ge_{1-y}Sn_y$ material system offers: (i) a tunable $Ge_{1-y}Sn_y$ bandgap by varying Sn incorporation while simultaneously maintaining lattice-matching with the underlying virtual substrate, *e.g.*, $In_xAl_{1-x}As$; (ii) carrier confinement within $Ge_{1-y}Sn_y$ for electronic (*i.e.*, electronic transport only through the GeSn material when it has been deposited on a large bandgap buffer, such as $In_xAl_{1-x}As$) and photonic (*i.e.*, the different refractive indices of $Ge_{1-y}Sn_y$ and $In_xAl_{1-x}As$) applications; (iii) potential as a source material in $Ge_{1-y}Sn_y/In_xGa_{1-x}As$ and similar heterojunction-based, ultra-low voltage tunnel transistor; [22-26] (iv) high responsivity when used as a photodetector material; [1, 27-31] (v) compatibility with Si CMOS technology; [32-38] and (vi), increased mobility due to a lower effective mass (m_{eff}) (high ON current, and therefore the opportunity for circuit-level scaling at low voltages). In light of the aforementioned advantages,

a. *Advanced Devices & Sustainable Energy Laboratory (ADSEL), Bradley Department of Electrical and Computer Engineering, Virginia Tech, Blacksburg, Virginia 24061, USA. E-mail: mantu.hudait@vt.edu; Fax: 540-231-3362; Tel: 540-231-6663*
b. *National Renewable Energy Laboratory, Golden, Colorado 80401, USA*

This journal is © The Royal Society of Chemistry 2022

J. Mater. Chem. C, 2022, **00**, 1-13 | **1**

researchers have been aggressively investigating epitaxial $Ge_{1-y}Sn_y$ on Si and Ge/Si,[1-18] and $Ge_{1-y}Sn_y$ on amorphous materials, for the development of the next generation of photodetectors and lasers. However, without an intermediate buffer layer between the epitaxial $Ge_{1-y}Sn_y$ and the Ge/Si substrate (the lattice-mismatch between GeSn and Si), device performance suffers due to the presence of defects and dislocations[39] in the active $Ge_{1-y}Sn_y$ region. In order to mitigate the propagation of lattice-mismatch-induced defects and dislocations, a lattice-matched buffer layer is recommended so as to improve material quality, and hence, the carrier lifetime in $Ge_{1-y}Sn_y$ materials. Thus, understanding carrier lifetime as a function of Sn composition in $Ge_{1-y}Sn_y$ alloys is essential for development of more efficient optoelectronic devices.

A reliable photodetector or laser structure requires a) an insignificant bandgap change with temperature, b) wavelength tunability with minimal change in design parameters, c) high carrier lifetime and reduced lattice-mismatch-induced junction leakage current, and d) increased band offsets between active channel (*e.g.*, $Ge_{1-y}Sn_y$) and barrier (*e.g.*, $In_xAl_{1-x}As$) material. Current strategies for Si-compatible optoelectronics rely on direct growth of SiGeSn or $Ge_{1-y}Sn_y$ on Si substrate, but this results in a lattice-mismatch induced defects and dislocations, which can severely impact carrier lifetime as well as junction leakage. Carrier lifetimes in $Ge_{1-y}Sn_y$ materials are expected to increase when grown on lattice-matched $In_xAl_{1-x}As$ intermediate buffers, wherein defects and dislocations can be reduced to negligible levels, as opposed to the direct growth of $Ge_{1-y}Sn_y$ on Si.[40-49]

Lattice-matched $Ge_{1-y}Sn_y/In_xAl_{1-x}As$ heterostructures can reduce the defect induced junction leakage and increase carrier lifetime. Two design strategies are considered here to improve the $Ge_{1-y}Sn_y$ material quality compared to direct growth on Si: a) the thickness of the $Ge_{1-y}Sn_y$ epilayer on AlAs/GaAs substrate below the critical layer thickness, and b) the growth of $Ge_{1-y}Sn_y$ epilayer lattice-matched to $In_xAl_{1-x}As$ (no thickness constraints). In both cases, no strain relaxation-induced defects will be generated in the $Ge_{1-y}Sn_y$ material. Moreover, the growth temperature (although lying within a small window) of the $Ge_{1-y}Sn_y$ material on $In_xAl_{1-x}As$ permits another avenue for improving the $Ge_{1-y}Sn_y$ material quality. As such, these routes provide more tenable mechanisms for synthesizing device-quality $Ge_{1-y}Sn_y$ materials.

Figure 1a shows the bandgap and lattice constant as a function of Sn (or InAs) mole fraction in $Ge_{1-y}Sn_y$ (or $In_xAl_{1-x}As$) at 300 K and 10 K.[32, 50, 51] The vertical dash-dotted line represents the bandgap for 6% Sn in $Ge_{0.94}Sn_{0.06}$, whereas the dash-dotted horizontal line represents the lattice-matched alloy compositions for
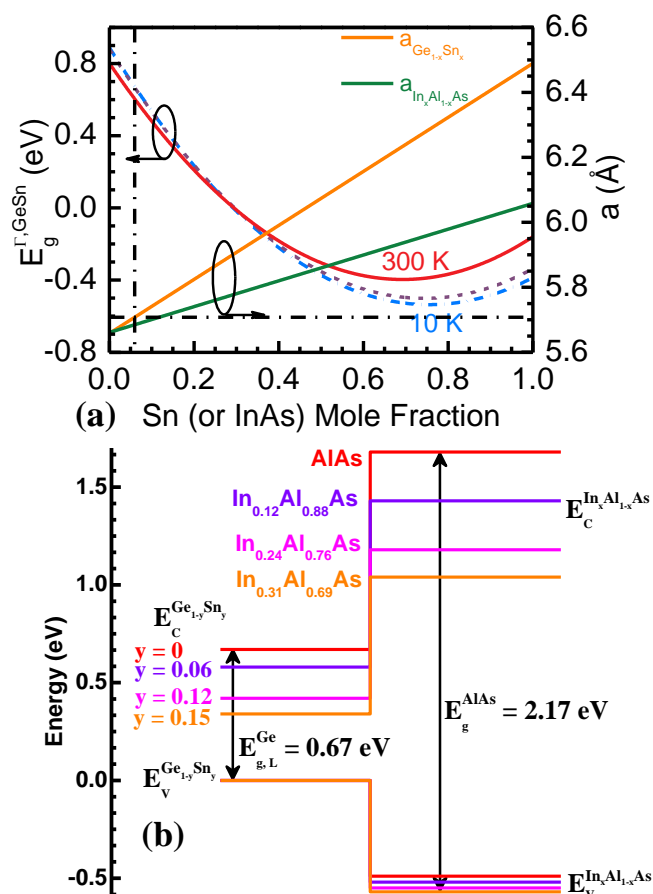
Fig. 1: (a) The bandgap and lattice constant *versus* Sn (or InAs) mole fraction in $Ge_{1-y}Sn_y$ (and $In_xAl_{1-x}As$) at 300 K and 10 K. (b) Schematic band alignment of lattice-matched $Ge_{1-y}Sn_y/In_xAl_{1-x}As$ heterostructures of selected Sn compositions at 300K. The vertical dash-dotted line in (a) represents the bandgap for 6% Sn in $Ge_{0.94}Sn_{0.06}$, and the dash-dotted horizontal line represents the lattice-matched compositions of 6% GeSn and $In_{0.12}Al_{0.88}As$, respectively. The 6% Sn mole fraction corresponds to $E_{g,GeSn}(\Gamma) \approx 0.6033$ eV, a 0.2 eV reduction (at $T = 300$ K) of the direct Ge E_g. The corresponding a_{GeSn} is equivalent to ~ 0.827% tensile strain Ge, with a compressive mismatch with respect to GaAs of ~ 0.96%.

$Ge_{0.94}Sn_{0.06}$ and $In_{0.12}Al_{0.88}As$, respectively. Noticeably, the bandgap of $Ge_{1-y}Sn_y$ remains almost constant with temperature until Sn = 35% and the most often targeted Sn compositional range for photodetector and laser applications is < 40%, due to the need for ultra-low growth temperatures (< 150°C) and spontaneous Sn segregation. Hence, by exploiting the $Ge_{1-y}Sn_y/In_xAl_{1-x}As$ heterostructure, $Ge_{1-y}Sn_y$-based tunable-wavelength photodetector and laser structures could be realized that would address many of the aforementioned issues, such as prohibitively high defect and dislocation densities, and their associated reduction in minority carrier lifetime and increase in junction leakage. The reduced junction leakage can be achieved by growing a lattice-matched $In_xAl_{1-x}As$ barrier underneath the $Ge_{1-y}Sn_y$ active region, and increased band offsets between $Ge_{1-y}Sn_y$ and In_xAl_{1-}

2 | *J. Mater. Chem. C*, 2022, **00**, 1-13

This journal is © The Royal Society of Chemistry 2022

$_x$As (*e.g.*, ΔE_V = 0.49 eV and ΔE_C = 1.01 eV for Ge/AlAs)[56] for electronic transport. Figure 1b shows the schematic of the band alignment of $Ge_{1-y}Sn_y/In_xAl_{1-x}As$ heterostructure with selected Sn compositions from 0 to 15%. The band alignment of the starting Ge/AlAs[56] and ε-Ge/In$_{0.26}$Al$_{0.74}$As[52] heterostructures, experimentally demonstrated *via* x-ray photoelectron spectroscopy were used. Moreover, the change in ΔE_V was relatively insignificant compared to ΔE_C with increasing In compositions in $In_xAl_{1-x}As$. The high band offsets, ΔE_C and ΔE_V at each lattice-matched $Ge_{1-y}Sn_y/In_xAl_{1-x}As$ heterostructure, indicates superior carrier confinement.

Although, extensive work has been performed in the direct integration of $Ge_{1-y}Sn_y$ on Si, there is a lack of literature on minority carrier lifetimes in $Ge_{1-y}Sn_y$ materials as a function of Sn alloy composition. Therefore, *this paper* highlights the material synthesis, structural analysis, and carrier lifetimes of epitaxial $Ge_{1-y}Sn_y$ layers on (100)GaAs substrates (with intermediate AlAs large-bandgap buffers) as (i) a function of Sn composition and lattice-matched $Ge_{0.94}Sn_{0.06}/In_{0.12}Al_{0.88}As$ heterostructure, (ii) function of growth temperature for a nominally fixed Sn composition, (iii) $Ge_{1-y}Sn_y$ epilayer thickness, and (iv) surface roughness. Without the *in-situ* growth capability provided by the interconnected, dual-chamber molecular beam epitaxy (MBE) process used herein, the oxidation of the $In_xAl_{1-x}As$ virtual substrate prior to $Ge_{1-y}Sn_y$ epitaxy would degrade the heterointerfacial lattice coherence, and thereby introduce deleterious crystalline defects into the $Ge_{1-y}Sn_y$ active region. Carrier lifetimes of 150 ns - 450 ns were measured for the 3-6% $Ge_{1-y}Sn_y$ epilayers using microwave photoconductive decay (*μ*-PCD) technique.[53, 54] Considering the many advantages of the $Ge_{1-y}Sn_y$ material system, as previously outlined, wide-spread device applications are possible if device-quality, tunable-composition epitaxial $Ge_{1-y}Sn_y$ materials can be realized through intelligent design of the underlying high-bandgap $In_xAl_{1-x}As$ buffer.

Experimental

A: Materials synthesis

Epitaxial $Ge_{1-y}Sn_y$ layers with varying Sn compositions from 0% to 6% were grown on semi-insulating (100)GaAs substrates that were 2° off towards <110> direction (with or without an intermediate AlAs buffer layer) using an ultra-high vacuum interconnected, dual-chamber MBE system with separate reactors for group IV and group III-V materials. The interconnected growth chambers minimize the atomic interdiffusion at the Ge/AlAs[55] and strained Ge/InAlAs heterointerfaces.[56] GeSn with 6% Sn composition was grown on graded

$In_xAl_{1-x}As$ buffers starting from GaAs substrate. 7N high-purity Ge (American GMG Incorporated, United Mineral and Chemical Corporation) and 6N high-purity Sn (American GMG Incorporated) elemental source materials were used for this work. An *in-situ* reflection high energy electron diffraction (RHEED) module connected to the III-V reactor was used to monitor the GaAs substrate oxide desorption process, and the surface reconstruction of the III-V epilayers (*i.e.*, GaAs, AlAs, and graded $In_xAl_{1-x}As$ buffer) during growth. Likewise, the surface reconstruction of the as-grown Ge and $Ge_{1-y}Sn_y$ films were investigated following $Ge_{1-y}Sn_y$ epitaxy and transfer of the sample(s) from the group IV reactor to the group III-V reactor. This *in-situ* growth and analysis capability permitted the examination of the surface reconstruction for representative GaAs, Ge and $Ge_{0.97}Sn_{0.03}$ samples. The GaAs substrate oxide desorption was performed at 750°C under an arsenic flux of ~10^{-5} Torr prior to reducing the temperature to 650°C for GaAs homoepitaxy. The temperature referred to herein was the thermocouple temperature. After the growth of the 250 nm GaAs homoepitaxial buffer, different thicknesses of AlAs (*see* Figure 2 below) were grown at 650°C (on a per-structure basis) prior to $Ge_{1-y}Sn_y$ epilayer growth. The 750 nm thick linearly graded $In_xAl_{1-x}As$ metamorphic buffer was grown at 480°C in order to balance the different adatom mobilities of aluminium (Al) and indium (In) on the growth surface. The overshoot In composition of ~16% was incorporated within the graded $In_xAl_{1-x}As$ buffer (x→0.03-0.16→0.12) for efficient strain relaxation. After the graded $In_xAl_{1-x}As$ buffer growth, a 15 minute, 580°C annealing step was implemented under an arsenic flux of ~10^{-5} torr to provide thermal energy for annihilation of lattice-mismatch induced defects. After annealing the graded $In_xAl_{1-x}As$ buffer layer, a constant composition of 0.5 μm thick $In_{0.12}Al_{0.88}As$ layer was grown at 580°C, which is lattice-matched to a $Ge_{0.94}Sn_{0.06}$ epilayer. Each layer structure was cooled down below 200°C under a decreasing As_2 overpressure, and vacuum (~ 4×10^{-10} Torr) transferred to the group IV reactor for $Ge_{1-y}Sn_y$ epitaxy in the temperature ranges from 175°C to 250°C. The growth rate of the Ge film was calibrated to 0.1 Å/s. The Sn cell temperature was varied for different Sn compositions. After the growth of each $Ge_{1-y}Sn_y$ film with different thicknesses and Sn compositions, each sample was cooled down to 50°C at a ramp rate of 5°C/min prior to unloading from the group IV reactor in order to prevent the formation of defects due to the dissimilar thermal expansion coefficients between each layers studied here. The details of the growth procedure for epitaxial Ge on GaAs as well as on AlAs are reported elsewhere.[25, 26]

This journal is © The Royal Society of Chemistry 2022

J. Mater. Chem. C, 2022, **00**, 1-13 | **3**

B: Materials characterization

The crystalline quality, Sn composition, and epilayer relaxation of each heterostructure were characterized using high-resolution x-ray diffraction (HR-XRD). X-ray rocking curves (*i.e.*, ω-2θ scans) and RSMs were recorded using a PANalytical X-pert Pro system equipped with PIXcel and proportional detectors and a monochromatic Cu Kα (λ = 1.540597 Å) x-ray source. The Sn-induced strain-state (*i.e.*, originating from the misfit with the underlying GaAs, AlAs and InAlAs materials) in each $Ge_{1-y}Sn_y$ layer was determined by HR-XRD. The strain analysis and composition of each layer after x-ray measurement were performed following the methods described in Ref. 57. The surface roughness of selected samples was determined using a Bruker Dimension Icon atom force microscope (AFM) under tapping mode. Carrier lifetimes were evaluated by microwave photoconductivity decay method, wherein the sample conductivity due to the excess carriers generated by laser excitation (wavelength of 1500 nm) was monitored *via* the microwave power reflected from each sample surface. During measurement, each sample

The repetition rate of the laser was 10 pulses/s. The laser power at 1500 nm was 20 mW when measured on a power meter where the absorption disk was 20 mm in diameter. The injection level of carriers is on the order of 10^{12} cm^{-3}. PCD lifetimes were quantified for each $Ge_{1-y}Sn_y$ layer by fitting the decay curve after the optical excitation pulse was ended. The details of this measurement technique can be found elsewhere.[54]

Results and discussion

A: *In-situ* surface analysis *via* RHEED

Figure 2 shows the cross-sectional schematic of each epitaxial $Ge_{1-y}Sn_y$ heterostructure investigated in this work. These sample structures were carefully selected as a function of Sn composition, buffer layer material type, thickness of each $Ge_{1-y}Sn_y$ layer, and growth temperature. **Table I** shows the $Ge_{1-y}Sn_y$/III-V heterostructures, studied in this work. These growth parameters enabled us to achieve high bulk carrier lifetime. Prior to measuring the carrier lifetime of each sample, surface analysis was performed on selected samples. The surface
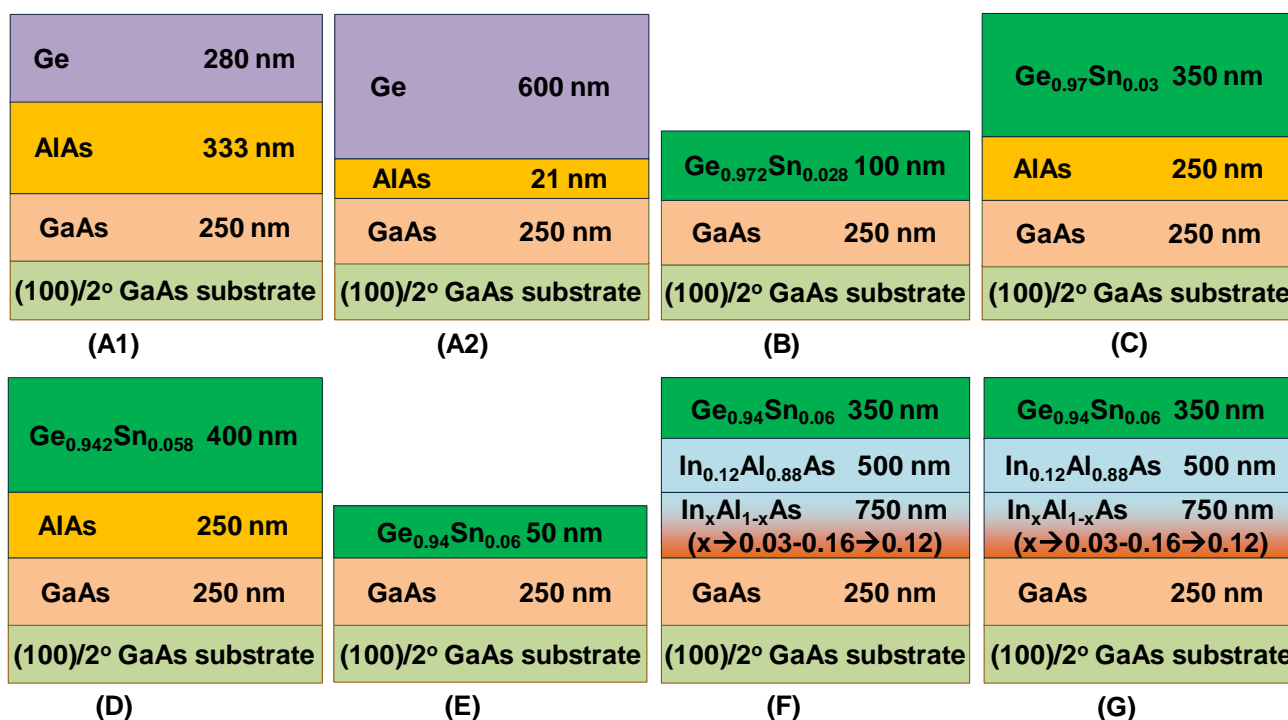
Fig. 2: Cross-sectional schematics of the $Ge_{1-x}Sn_x$/AlAs/(100)GaAs heterostructures investigated in this work: (**A1**) 280 nm thick epitaxial Ge layer on 333 nm AlAs buffer on semi-insulating (S. I.) GaAs substrate; (A2) 600 nm thick epitaxial Ge layer on 21 nm AlAs buffer; (**B**) 100 nm thick $Ge_{0.972}Sn_{0.028}$ on 250 nm GaAs buffer; (**C**) 350 nm thick $Ge_{0.97}Sn_{0.03}$ on 250 nm AlAs buffer; (**D**) 400 nm thick $Ge_{0.942}Sn_{0.058}$ on 250 nm AlAs buffer layer; (**E**) 50 nm thick $Ge_{0.94}Sn_{0.06}$ on 250 nm GaAs buffer; (**F-G**) 350 nm thick $Ge_{0.94}Sn_{0.06}$ on 500 nm thick lattice-matched $In_{0.12}Al_{0.88}As$/$In_xAl_{1-x}As$/GaAs buffer layer grown at 250°C and 175°C, respectively.

(dimensions $\sim$10 mm $\times$ 10 mm) was placed underneath the waveguide (WR42 for 20GHz, dimensions $\sim$ 4.3 mm $\times$10.7 mm), and the beam flux at this wavelength fills the waveguide. Each sample faces up and the laser excitation at this wavelength was incident from the top.

reconstruction of selected samples was studied using RHEED analysis. It is one of the most powerful *in-situ* characterization techniques used in MBE for the surface analysis of semiconductors during growth, as well as in the determination of epilayer growth rate. In this work,

4 | *J. Mater. Chem. C*, 2022, **00**, 1-13

This journal is © The Royal Society of Chemistry 2022

ARTICLE

Table I: Carrier lifetime in epitaxial Ge$_{1-y}$Sn$_y$/III-V heterostructures as a function of Sn composition.

Sample Label	Sn (%)	Buffer/substrate	Growth Temp (ºC)	Ge or GeSn thickness (nm)	Carrier lifetime (ns)	R^2 (linear regression)
A1 (Pseudomorphic)	0	AlAs/GaAs/2º-GaAs	400	280	91.20	0.98504
A2 (Pseudomorphic)	0	AlAs/GaAs/2º-GaAs	400	600	320.02	0.97751
B (Pseudomorphic)	2.8	GaAs/2º-GaAs	200	100	257.33	0.99292
C (Pseudomorphic)	3.0	AlAs/GaAs/2º-GaAs	200	350	220.35	0.98725
D (Partially relaxed)	5.8	AlAs/GaAs/2º-GaAs	200	400	150.90	0.94837
E (Pseudomorphic)	6.0	GaAs/2º-GaAs	195/190	50	468.06	0.99276
F (Lattice-matched)	6.0	In$_{0.12}$Al$_{0.88}$As/In$_x$Al$_{1-x}$As/GaAs/2º-GaAs	250	350	324.06	0.98155
G (Lattice-matched)	6.0	In$_{0.12}$Al$_{0.88}$As/In$_x$Al$_{1-x}$As/GaAs/2º-GaAs	175	350	208.94	0.95271

RHEED patterns were recorded at different stages of the growth process in order to understand the surface morphology of the as-grown Ge and Ge$_{0.97}$Sn$_{0.03}$ materials. The surface reconstruction of the (100)GaAs substrate, epitaxial Ge, and epitaxial Ge$_{0.97}$Sn$_{0.03}$ was examined using *in-situ* RHEED analysis during growth, as shown in Figure 3. Figure 3(i) shows a representative RHEED pattern obtained from the surface of a (100)GaAs substrate (or homoepitaxial layer) along the [110] and [1$\bar{1}$0] azimuthal directions, which exhibited a streaky (2×4) surface reconstruction. From Figure 3(i), one can find that the main and higher-order diffraction points exhibited a high degree of elongation and relative intensity, indicative of a smooth surface morphology during growth. Figures 3(ii) and 3(iii) similarly display the RHEED patterns from the surface of Ge and Ge$_{0.97}$Sn$_{0.03}$ epilayers, respectively, recorded along the [110] and [1$\bar{1}$0] azimuths. An unintentionally-doped epitaxial Ge layer deposited on the (2×4) reconstructed (100)GaAs surface exhibited a streaky (2×2) surface construction, comparable to that of RHEED patterns reported earlier,[25, 57] and likewise indicative of 2D growth and a smooth surface morphology.[25, 58] As the group IV and group III-V MBE reactors used in this work were interconnected *via* an ultra-high vacuum transfer chamber, the epitaxial Ge$_{1-y}$Sn$_y$ layers were also transferred to the group III-V reactor for RHEED surface analysis post-growth. Streaky and sharp (2×2) RHEED patterns along the [110] and [1$\bar{1}$0] azimuths were observed from the surface of the Ge$_{0.97}$Sn$_{0.03}$ grown on (100)GaAs with an intermediate AlAs buffer layer, as shown in Figure 3(iii). In addition, the elongation and relative intensity of the main and higher-order diffraction points on the Ge$_{0.97}$Sn$_{0.03}$ surface were found to be greater than that seen in the Ge (2×2) surface reconstruction pattern, suggesting a smoother and more uniform surface morphology on the former, which will be validated using AFM analysis. Hence, the RHEED observations of the Ge$_{0.97}$Sn$_{0.03}$/AlAs heterostructure show similar RHEED patterns to those of unstrained and strained Ge

epilayers,[25, 58] but with elongated and more intense diffraction, suggestive of more uniform surfaces with lower surface roughness.
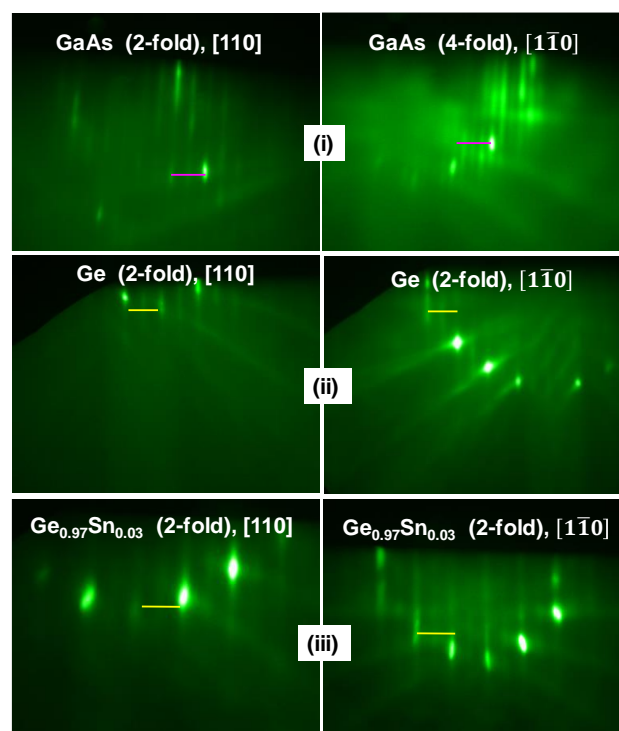
Fig. 3: The *in-situ* RHEED patterns from the surface of (i) a representative (100)GaAs substrate, (ii) epitaxial Ge, and (iii), epitaxial Ge$_{0.97}$Sn$_{0.03}$ (Sample C) on AlAs/(100)GaAs along the azimuth of [110]. The RHEED patterns exhibited streaky (2×4) and (2×2) surface reconstructions from the surface of (100)GaAs, and Ge or Ge$_{0.97}$Sn$_{0.03}$, respectively. Similar (2×2) RHEED patterns were obtained from the tensile-strained Ge epilayer surface grown on a In$_x$Ga$_{1-x}$As metamorphic buffer [25, 57]. The sharp and streaky RHEED patterns were indicative of high-quality Ge$_{0.97}$Sn$_{0.03}$ epitaxy with a smooth surface morphology.

B: Surface morphology *via* AFM

Characterization of surface roughness and demonstration of smooth surface morphologies, using AFM analysis, is a key indicator for pseudomorphic and metamorphic
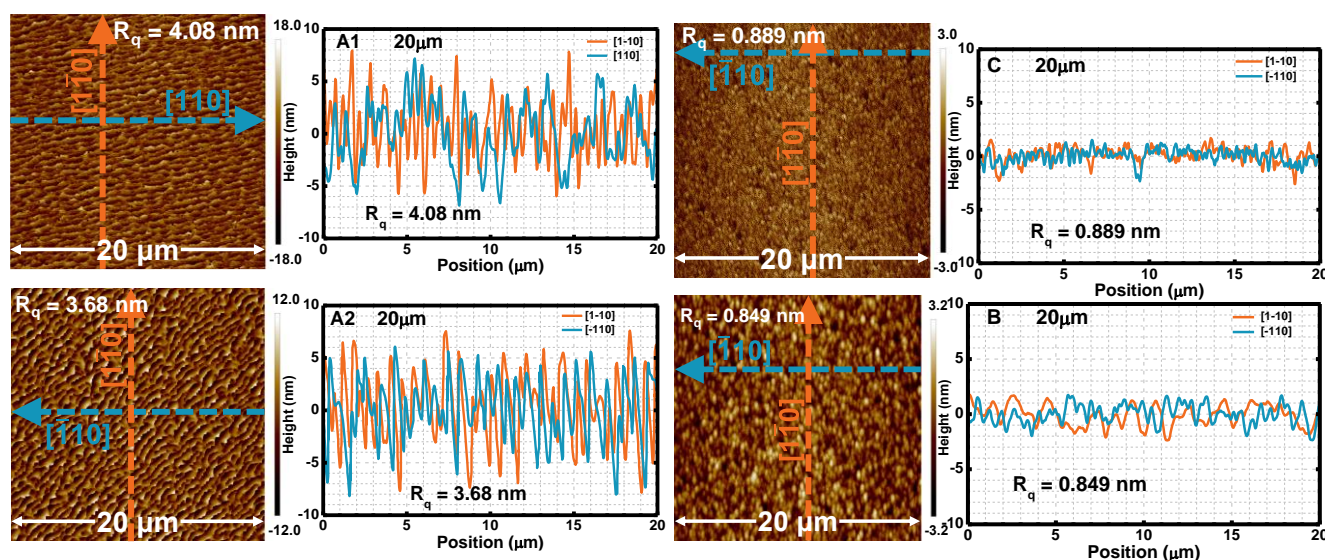
Fig. 4: AFM micrographs and corresponding line profiles from the surface of 20×20 μm^2 epitaxial 280 nm Ge (A1), 600 nm Ge (A2), 100 nm $Ge_{0.972}Sn_{0.028}$ (B), and 350 nm $Ge_{0.97}Sn_{0.03}$ (C) layers, demonstrating an RMS roughness of 8.89 Å over the 20×20 μm^2 scan area (Sample C; $Ge_{0.97}Sn_{0.03}$). A uniformly smooth surface morphology with a maximum peak-to-valley height of ~6 nm was likewise observed.

heterostructures. In the previous section, the observed $Ge_{0.97}Sn_{0.03}$ RHEED patterns suggested a smooth surface morphology for the $Ge_{0.97}Sn_{0.03}$ film, more so than that of the Ge surface due to the elongated and intense diffraction observed. Figure 4 shows the 20 $\mu m \times$ 20 μm AFM micrographs and corresponding line profiles taken along the two orthogonal [110] directions and recorded from the surfaces of 280 nm Ge (A1), 600 nm Ge (A2), 100 nm $Ge_{0.972}Sn_{0.028}$ (B) and 350 nm $Ge_{0.97}Sn_{0.03}$ (C). The superior surface morphology of the $Ge_{0.97}Sn_{0.03}$/AlAs/GaAs heterostructure, with a root mean square (*rms*) roughness of 8.89 Å, in contrast to the 3.68 nm or 4.08 nm *rms* roughness of the Ge/AlAs/GaAs structures, suggests surfactant-mediated-like growth kinetics during incorporation of Sn into the $Ge_{1-y}Sn_y$ epilayer. The $Ge_{0.97}Sn_{0.03}$ surface roughness observed in this work was found to be in agreement with similar $Ge_{1-y}Sn_y$ surface morphologies reported in Refs. [59, 60]. Although reduced $Ge_{1-y}Sn_y$ growth temperatures, such as those used in this work, would limit the surface adatom mobility, in turn lowering the surface roughness, it is also expected to promote point defects.[42, 61] Therefore, a higher growth temperature would be preferable in order to mitigate the point defects at the cost of an increase in surface roughness. In the current work, no attempt was made to optimize the surface morphology as a function of growth parameters, such as growth temperature, growth rate, Sn content, or thickness of the $Ge_{1-y}Sn_y$ epilayers. However, the low *rms* roughness of the $Ge_{0.97}Sn_{0.03}$ surface suggests a high crystalline quality with high carrier lifetime.

C: Compositional and structural analysis *via* x-ray analysis

$Ge_{0.972}Sn_{0.028}$/GaAs and $Ge_{0.97}Sn_{0.03}$/AlAs heterostructures - The $Ge_{1-y}Sn_y$/AlAs (or GaAs) heterostructure crystal quality, Sn composition, and epilayer relaxation and strain-states were characterized using HR-XRD analysis. X-ray rocking curves (*i.e.*, ω-2θ scans) were recorded using a PANalytical X-pert Pro system equipped with PIXcel and proportional detectors. Figure 5 shows the x-ray analysis of epitaxial $Ge_{0.97}Sn_{0.03}$ layers grown on (100)GaAs substrates (a) without and (b) with an intermediate AlAs buffer layer by MBE. This large bandgap AlAs buffer is expected to serve as a parallel conduction barrier layer (for carrier transport), or as the epitaxial release layer for the lift-off of the overlying $Ge_{1-y}Sn_y$ epilayer from the GaAs substrate. Figures 5(a)and 5(b) show the experimental (measured, red) and simulated (blue) x-ray rocking curves for the $Ge_{0.972}Sn_{0.028}$/(100)GaAs and $Ge_{0.97}Sn_{0.03}$/AlAs/(100)GaAs heterostructure, respectively, revealing abrupt interfaces for each heterostructure as indicated by the presence of Pendellösung oscillations. In addition, reciprocal space maps (RSMs) of these structures show the reciprocal lattice points (RLPs) contours of the $Ge_{0.97}Sn_{0.03}$, AlAs, and GaAs lattices. The Q_z separation of the RLPs in the (004) RSMs show the compressively strained nature of the $Ge_{1-y}Sn_y$ epilayer with respect to either the GaAs substrate or AlAs buffer. The RLPs of the different constituent materials were found to be in alignment along the Q_z-axis, indicating the fully-strained (*i.e.*, pseudomorphic) state of the $Ge_{0.97}Sn_{0.03}$ epilayer. It

(a) 100 nm $Ge_{0.972}Sn_{0.028}$/(001)GaAs

(b) 350 nm $Ge_{0.97}Sn_{0.03}$/250 nm AlAs/(001)GaAs
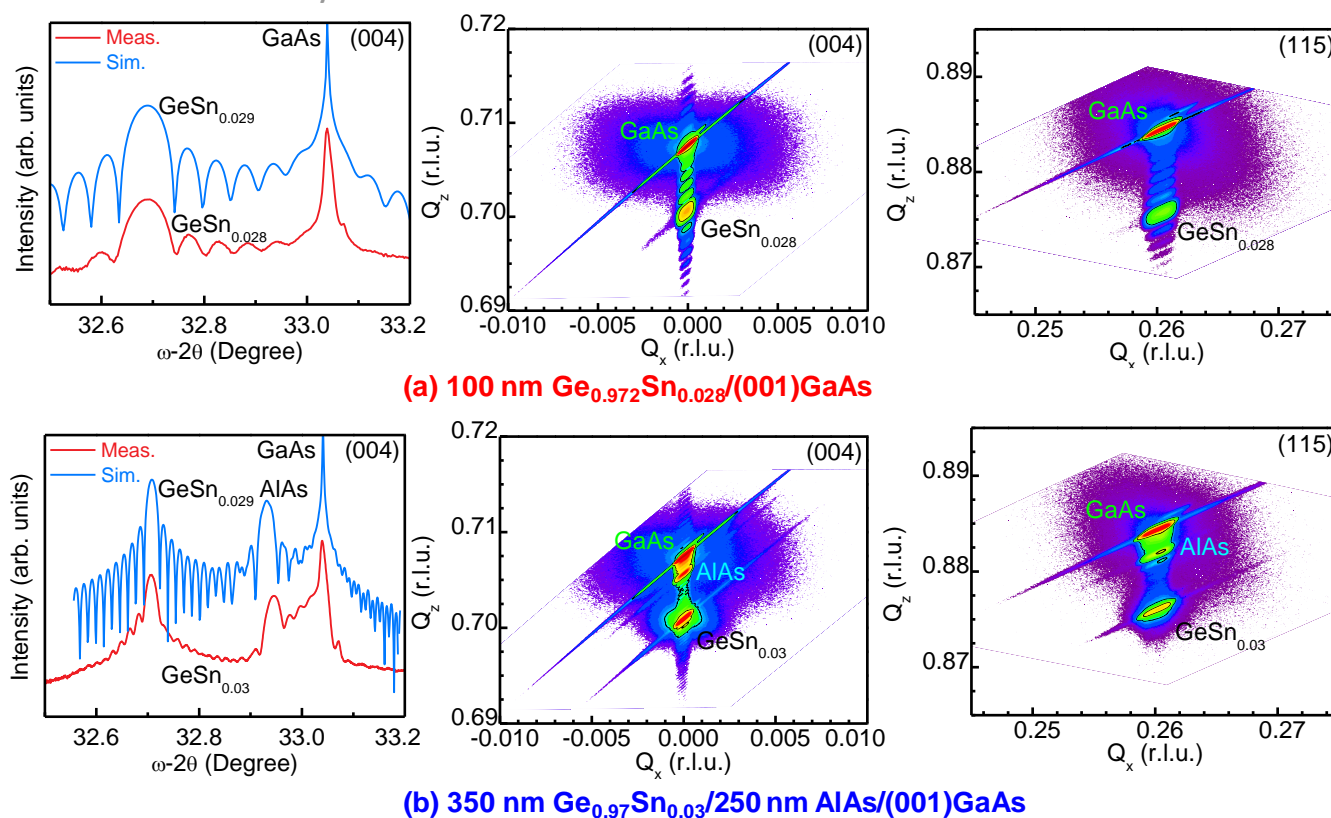
Fig. 5: X-ray rocking curves of measured (red) and simulated (blue) (a) $Ge_{0.972}Sn_{0.028}$ on (100)GaAs (Sample B), as well as (b) $Ge_{0.97}Sn_{0.03}$ on (100)GaAs (Sample C) with an intermediate AlAs buffer layer, showing Pendellösung oscillations indicative of superior $Ge_{1-y}Sn_y$ material synthesis and smooth heterointerfaces. Symmetric (004) and asymmetric (115) reciprocal space maps of the $Ge_{0.972}Sn_{0.028}$ ($Ge_{0.97}Sn_{0.03}$) epitaxial layers on (100)GaAs substrates, revealing pseudomorphic heterointerfaces as shown by the Q_z alignment of the GaAs, AlAs, and GeSn reciprocal lattice contours in both the (004) and (115) scans. The $Ge_{1-y}Sn_y$ peaks show a smaller Bragg angle than the (100)GaAs substrate, indicating a larger out-of-plane and smaller in-plane lattice constant. The compressive strain-state of the $Ge_{1-y}Sn_y$ epilayer was determined to be ~ 0.53% with respect to the (100)GaAs substrate. The corresponding a_{GeSn} is equivalent to ~ 0.44% tensile-strained Ge.

should be noted that the low misfit of the ~$Ge_{0.97}Sn_{0.03}$/AlAs system, besides the limited 100 nm and 350 nm $Ge_{1-y}Sn_y$ thickness, permitted the growth of these fully-strained heterostructures absent of quantifiable relaxation. As such, one should not expect lattice-mismatch-induced defects at the heterointerfaces of the $Ge_{1-y}Sn_y$/AlAs or GaAs system for low Sn compositions ($\leq 3\%$). Similar analysis was performed on a 400 nm-thick $Ge_{1-y}Sn_y$ epitaxial layer grown on GaAs with an intermediate 250 nm-thick AlAs buffer.

$Ge_{0.94}Sn_{0.06}$/$In_{0.12}Al_{0.88}As$/$In_xAl_{1-x}As$ heterostructure – Figures 6a and 6b show the recorded symmetric (004) and asymmetric (115) RSMs, respectively, from the $Ge_{0.94}Sn_{0.06}$/$In_{0.12}Al_{0.88}As$/$In_xAl_{1-x}As$/GaAs structure, highlighting the RLP centroid for each epilayer. The Sn composition from the measured RSMs was found to be ~6%. HR-XRD data reveal that the 350 nm thick $Ge_{0.94}Sn_{0.06}$ epilayer is indeed lattice-matched with respect to the $In_{0.12}Al_{0.88}As$ virtual substrate (VS). As can be seen from the symmetric (004) RSM shown in Fig. 6a, the in-plane lattice constant of $Ge_{0.94}Sn_{0.06}$ layer is matched with the upmost composition $In_{0.12}Al_{0.88}As$ of the graded $In_xAl_{1-x}As$ buffer

layer. Fig. 6b further confirms the lattice-matched $Ge_{0.94}Sn_{0.06}$/$In_{0.12}Al_{0.88}As$ heterostructure where the RLPs of both $Ge_{0.94}Sn_{0.06}$ and $In_{0.12}Al_{0.88}As$ layers are on top of each other. The overshoot In composition of 16% embedded into linearly graded $In_xAl_{1-x}As$ buffer (below the $In_{0.12}Al_{0.88}As$ RLP) is to relax the graded $In_xAl_{1-x}As$ buffer layer. Further examination of (115) RSM (Fig. 6b)
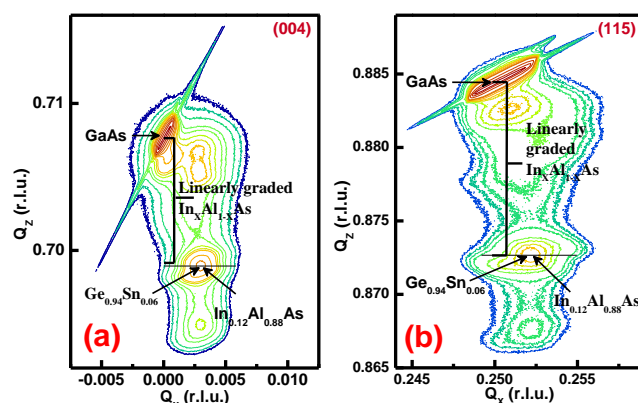
Fig. 6: RSMs taken along the (a) (004) and (b) (115) orientations. These RSMs support the lattice-matched epitaxy of 350 nm thick $Ge_{0.94}Sn_{0.06}$ on $In_{0.12}Al_{0.88}As$ buffer layer, which is expected to increase the carrier lifetime in GeSn layer (Table I, Sample F).

reveals a close alignment in the Q_x components of the $Ge_{0.94}Sn_{0.06}$ and $In_{0.12}Al_{0.88}As$ RLPs, indicative of coherent lattice-matched epitaxy. Moreover, the Q_x-Q_z symmetry of the GeSn RLP suggests a uniform crystallinity absent of substantial mosaicity-inducing crystal defect scattering. Likewise, the narrow, symmetric nature of the $In_xAl_{1-x}As$ RLP indicates dislocation-minimal constant composition growth, signifying a strong confinement of mismatch-induced defects in the linearly graded $In_xAl_{1-x}As$ buffer. Similar analysis was performed on a 50 nm-thick $Ge_{0.94}Sn_{0.06}$ epitaxial layer grown on GaAs with an intermediate 25 nm-thick Ge buffer, shown below.

$Ge_{0.94}Sn_{0.06}$/GaAs heterostructure – Figures 7a and 7b show the measured symmetric (004) and asymmetric (115) RSMs, respectively, from the 50 nm thick $Ge_{0.94}Sn_{0.06}$ layer directly grown on GaAs substrate with a 25 nm thick Ge buffer layer. The RLP of each layer and the substrate is clearly visible. The (115) RSM shows the compressively strained $Ge_{0.94}Sn_{0.06}$ layer, as expected. The RLP contour is broad as compared to 350 nm thick $Ge_{0.94}Sn_{0.06}$ material grown on lattice-matched $In_{0.12}Al_{0.88}As$ buffer layer, as shown in Fig. 6. The carrier lifetime is expected to increase in this $Ge_{0.94}Sn_{0.06}$ epitaxial layer due to no defects and dislocations generated *via* strain relaxation.
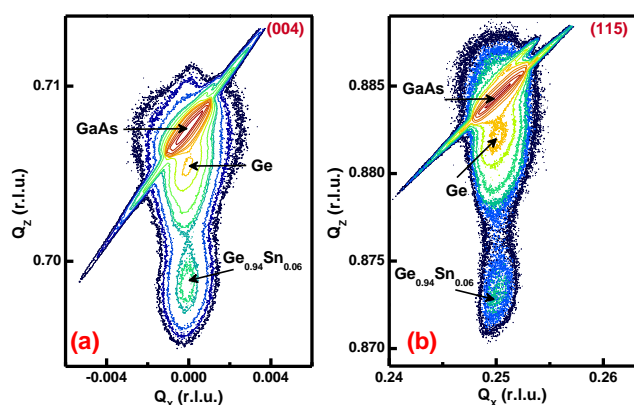
Fig. 7: RSMs taken along the (a) (004) and (b) (115) orientations. These RSMs support the compressively strained $Ge_{0.94}Sn_{0.06}$ on (100)GaAs substrate, which is expected to increase the carrier lifetime in $Ge_{0.94}Sn_{0.06}$ layer (Table I, Sample E).

D: Carrier lifetimes *via* PCD

Carrier lifetime is a common material parameter used in the evaluation of semiconductor material quality, similar to Hall mobility, due to the sensitivity of carrier lifetime to defects and dislocations. Particularly for photonic and optoelectronic materials, such as $Ge_{1-y}Sn_y$, the evaluation of carrier lifetime is as important as carrier mobility. Correspondingly, different measurement techniques, such as temperature dependent photoluminescence, microwave reflection and

transmission probing, and non-contact PCD, were developed over the years. [44, 45, 48, 49, 53, 54, 61, 62] In this work, the minority carrier recombination properties in $Ge_{1-y}Sn_y$/InAlAs and $Ge_{1-y}Sn_y$/GaAs or AlAs heterostructures were probed at 300 K using the ultrahigh frequency microwave reflection PCD analysis at the National Renewable Energy Laboratory (NREL). The $Ge_{1-y}Sn_y$ minority carrier recombination properties were studied as a function of $Ge_{1-y}Sn_y$ epilayer thickness, surface roughness, and Sn alloy composition. An excitation wavelength of 1500 nm was used, and the carrier lifetimes were quantified by fitting the decay curve after a short ~3 ns optical excitation pulse ended. An overview of the PCD measurement technique and measurement setup used herein can be found elsewhere. [53, 54, 62] Figure 8 shows the PCD signal obtained from the $Ge_{1-y}Sn_y$/InAlAs and $Ge_{1-y}Sn_y$/GaAs or AlAs heterostructures measured using a 1500 nm excitation wavelength. The absorption coefficient of Ge at 1500 nm is 4×10^3 cm^{-1}, and the penetration depth at this wavelength is much larger than the thickness of the $Ge_{1-y}Sn_y$ epitaxial layers studied here. One can find from Figure 8 that there are two-time scale windows (highlighted by the two shaded areas, I and II) for carrier recombination. The fast (I) time scale for initial relaxation is due to the recombination of excess photogenerated carriers at the surface. Surface recombination cannot be avoided, but can be minimized for samples with lower surface roughness, or passivated samples. Photogenerated carrier diffusion could occur during this time frame, following carrier generation, but
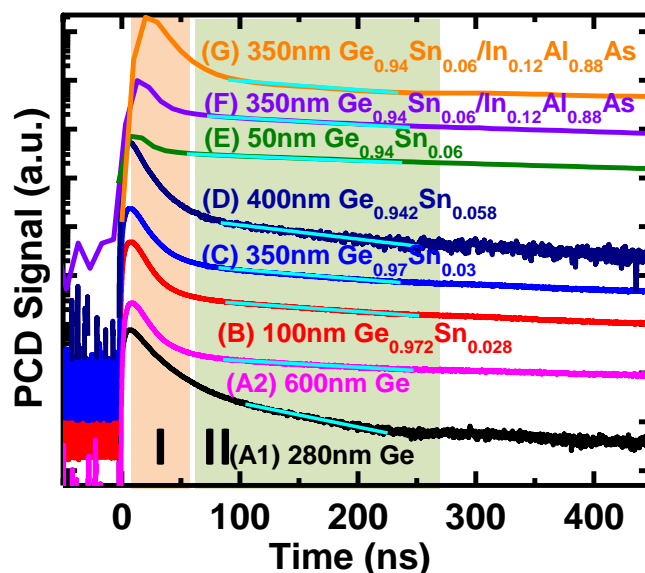
Fig. 8: PCD data at 300 K obtained from the $Ge_{1-y}Sn_y$/III-V heterostructures with different thicknesses, wherein the excitation at a 1500 nm wavelength was applied from the front side of each heterostructure. The figure also shows the fits to the data (Cyan) for each PCD signal, wherein the effective carrier lifetime was determined (Region II) for each sample studied here. The initial PCD signal decreases sharply from 0 ns to 50 ns after excitation (Region I). All data has been offset for clarity

8 | *J. Mater. Chem. C*, 2022, **00**, 1-13

This journal is © The Royal Society of Chemistry 2022

the rate of diffusion would be smaller due to surface recombination. However, these excess carriers would diffuse into the bulk of the sample, depending on the excitation energy subsequent to initial surface recombination.[54] In addition, surface recombination would be more pronounced for samples with higher surface roughness. The PCD measurement technique is able to monitor excess carriers deep into the bulk and the carrier lifetime, which is the bulk lifetime, can be extracted from the measured decay signal. For samples with higher surface roughness, excess carriers can recombine quickly, leading to a fast initial PCD decay signal. The slower (II) time scale is correlated to the bulk lifetime of photogenerated carriers *via* Shockley-Read-Hall (SRH) recombination, which is related to carriers trapping on impurities or defects. By fitting the PCD signal (V_{PCD}) to $V_{PCD} = A.exp\left(-\dfrac{t}{\tau_{PCD}}\right)$ within the low-level injection regime, shown in the second shaded area (II), as indicated in Figure 8, the PCD lifetimes (τ_{PCD}) were extracted, where the pre-exponential factor A is a constant and t is the photoconductive decay time. Figure 9 shows the extracted bulk lifetime as a function of Sn composition in the investigated $Ge_{1-y}Sn_y$ layers. One can observe three lifetime trends: (i) region I, related to the change in Ge thickness from 280 nm to 600 nm; (ii) region II, related to the reduction in surface roughness from 4 nm to 0.8 nm; and (iii), region III, related to 6% Sn alloy composition within the $Ge_{1-y}Sn_y$ epilayers. Table I shows the $Ge_{1-y}Sn_y$ epitaxial layer details along with growth temperature, buffer layer and measured carrier lifetimes as determined using the PCD method at NREL.

From Figure 9 (Regions I, II), one can find that τ_{PCD} increased from 90 ns (A1) to 320 ns (A2), representing a $3.5\times$ increase in bulk lifetime, when the Ge film thickness was increased from 280 nm to 600 nm (a $2\times$ increase) for the same excitation wavelength. The increased bulk lifetime with the increase in Ge film thickness is due to less relative surface and interface recombination in the thicker sample. It should be noted that the surface roughness of both samples was virtually identical (4 nm vs 3.7 nm). The impact of the surface roughness on the bulk lifetime of Ge and $Ge_{1-y}Sn_y$ epilayers is also shown in Fig. 9 (Region II). The carrier lifetime is higher in GeSn samples with lower surface roughness (B & C) than Ge layer (A1), an essential criterion for photonic or electronic device applications. However, GeSn sample (D) with partially relaxed (~16%), could create defects and dislocations inside the film or interface, which resulted in the decreased bulk lifetime. However, the carrier lifetime (Region III) was enhanced by growing pseudomorphic (thinner layer, E) and lattice-matched $Ge_{0.94}Sn_{0.06}/In_{0.12}Al_{0.88}As$ structure
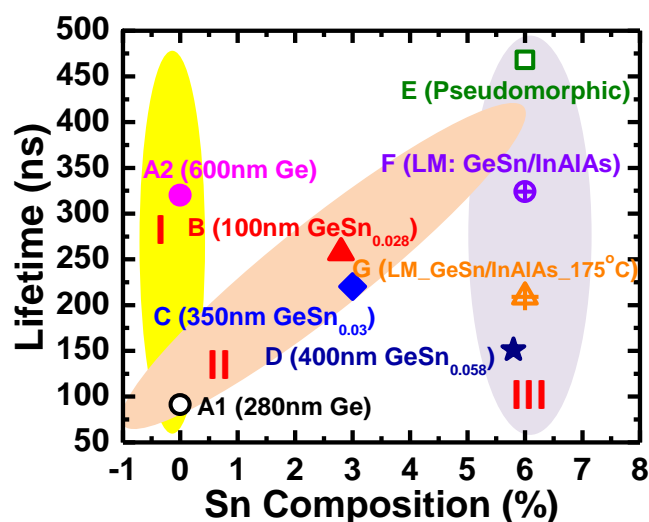
Fig. 9: Carrier lifetime *vs.* Sn composition for the $Ge_{1-y}Sn_y/III$-V heterostructures. The carrier lifetime increased with increasing Ge epilayer thickness (A1 to A2), due to less overlap between surface and interface effects. The lifetime also increased with reducing surface roughness (A1 to C) and pseudomorphic (E) or lattice-matched (F) composition. It decreased in lower temperature growth (G) and partially relaxed case (D). The measured lifetime was above 300 ns for the lattice-matched $Ge_{0.94}Sn_{0.06}$ layer on $In_{0.12}Al_{0.88}As/In_xAl_{1-x}As/GaAs$.

(F: no thickness constraints), which is needed for photodetector development. One can find that the lifetime is increased from 150 ns to 324 ns at 6% Sn composition by minimizing the dislocations at the interface of $Ge_{0.94}Sn_{0.06}/In_{0.12}Al_{0.88}As$ (F).

The μ-PCD technique measures the carrier lifetime resulting from parallel intrinsic and extrinsic recombination processes. It is based on the change in local conductance when the laser source generates excess carriers in the sample. The reflected microwave signal from the sample surface is measured, and the reflected intensity is changed compared to the incident intensity due to the change in the effective refractive index of the sample (which is due to the change in conductance). In the carrier recombination dynamics, there are mainly three recombination processes that can occur: band-to-band recombination, Auger recombination and trap-assisted or Shockley Read Hall (SRH) or non-radiative recombination, for determination of carrier lifetime in a semiconductor. In addition, the bulk recombination rate (R), which depends on the number of excess carriers and type of semiconductor (direct versus indirect), is important. In moderately doped semiconductor, Auger recombination process is neglected (at high carrier density, the lifetime is controlled by Auger combination) and then left with two recombination processes. Another important parameter is the level of carrier injection during measurement: low-level (*ll*) where excess minority carrier density is low compared with majority carrier density, $\Delta p \ll n_o$ (GeSn samples are *n*-type with

doping density of $\sim 3 \times 10^{18}$ cm^{-3} measured via Hall effect with van der Pauw method) and high-level (hl), $\Delta p \gg n_o$. At low level injection ($\sim 10^{12}$ cm^{-2} in this work), the carrier recombination lifetime (τ_r) is defined as,[63]

$$\tau_r = \frac{\Delta p}{R} = \frac{1}{\tau_{rad}^{-1} + \tau_{SRH}^{-1} + \tau_{Auger}^{-1}} \approx \frac{1}{\tau_{rad}^{-1} + \tau_{SRH}^{-1}}, \quad (1)$$

$$\tau_{rad}(ll) = \frac{1}{Bn_o}; \; \tau_{SRH}(ll) \approx \tau_p; \tau_{rad}(hl) = \frac{1}{B\Delta p}, \quad (2)$$

where τ_{rad} is the radiative lifetime, τ_{SRH} is the SRH lifetime, τ_p is the minority carrier lifetime, Δp is the excess minority carrier density, and B is the radiative recombination coefficient. Since the B value is unknown for Ge$_{1-y}$Sn$_y$ material, it is modest to assume that it lies between the Ge[63] and InAs[64] semiconductors to determine the τ_{rad} for Ge$_{1-y}$Sn$_y$ material. The τ_{rad} for ll or hl injection is in microseconds to nanoseconds for these semiconductors. The carrier lifetimes in Ge$_{1-y}$Sn$_y$ materials, reported in Table I, are in hundreds of nanoseconds implying that they are SRH limited. If the threading dislocation density is high within the film, then the carrier lifetime would be reduced.[65] Recently reported carrier lifetime of 217 ps at 20 K for 350 nm Ge$_{0.875}$Sn$_{0.125}$ film on Ge-buffered Si (at the laser excitation fluence of $\sim 10^{14}$ cm^{-2}) using the time-resolved photoluminescence spectroscopy is limited by excitons bound to defects or other defects-based recombination. It is evident that the integrated intensity at 20 K is significantly higher than that at 300 K, indicating non-radiative recombination processes were present.[40] Thus, the lattice-matched Ge$_{1-y}$Sn$_y$/ InAlAs material offers higher carrier lifetime due to low defect density.

The high carrier lifetime in Ge$_{1-y}$Sn$_y$ materials measured in this work can increase the internal quantum efficiency (IQE) of a laser diode.[46] In the case of $\sim 7\%$ Sn alloy composition in Ge$_{1-y}$Sn$_y$, which is equivalent to $\sim 1\%$ tensile strain in Ge, the theoretical IQE is 0.001 for a lifetime of 1 ns and the IQE improves to 0.1 for a lifetime of 100 ns, which shows an order of magnitude increase in IQE corresponding to an order of magnitude increase in lifetime.[46] This implies that samples (A1 – G) would provide a theoretical IQE in the range of 0.05 to 0.5, whereas sample E with 6% Ge$_{0.94}$Sn$_{0.06}$ grown on a lattice-matched In$_{0.12}$Al$_{0.88}$As buffer would provide a maximum IQE of ~ 0.5. Also, the threshold current density (J_{th}) for a direct bandgap Ge$_{1-y}$Sn$_y$ material can drop to ~ 1 kA/cm^2 for a lifetime beyond 100 ns.[46] Samples A1 and A2 with 0% Sn as well as samples B and C with 3% Sn would have a high J_{th} than samples D-G with 6% Sn, which are closer to a direct bandgap material. Hence, monolithic integration of variable Sn alloy compositional Ge$_{1-y}$Sn$_y$ materials on lattice-matched In$_x$Al$_{1-x}$As with high carrier lifetime would aid in realizing Si-compatible lasers and photodetectors.

Conclusions

Group IV-based Ge$_{1-y}$Sn$_y$ materials have recently shown great promise for infrared detection. To that end, high carrier lifetimes are desirable for enhancing the detection limit and photodetector efficiency. In this work, carrier lifetimes in epitaxial Ge and tunable Sn composition Ge$_{1-y}$Sn$_y$ materials were experimentally determined on (100)GaAs substrates with and without an intermediate AlAs buffer. A dual-chamber, solid-source molecular beam epitaxy deposition system with *in-situ* RHEED capability was used for Ge$_{1-y}$Sn$_y$ materials synthesis. Streaky and sharp (2×2) RHEED patterns along the [110] and [$1\bar{1}0$] azimuths were observed from the surface of Ge$_{0.97}$Sn$_{0.03}$, with elongated and intense primary and higher-order diffraction, particularly compared to epitaxial Ge, indicative of a smooth surface morphology. X-ray analysis, demonstrated pseudomorphic and lattice-matched growth on AlAs and In$_{0.12}$Al$_{0.88}$As buffer respectively, further substantiated by reciprocal space maps as well as abrupt heterointerfaces evident from the presence of Pendellösung oscillations. High effective carrier lifetimes of 150 ns to 450 ns were measured at room temperature for Ge$_{1-y}$Sn$_y$ epilayers as a function Sn composition, surface roughness, and layer thickness. The observed increase in carrier lifetime with increasing Ge layer thickness and reducing surface roughness, by incorporating Sn were explained. The increased carrier lifetime with increasing Sn was realized by synthesizing lattice-matched GeSn/InAlAs heterostructure as well as pseudomorphic growth of GeSn on GaAs substrates. Therefore, our monolithic integration of variable Sn alloy compositional Ge$_{1-y}$Sn$_y$ materials with high carrier lifetime opens avenues to realize electronic and optoelectronic devices.

Conflicts of interest

There are no conflicts to declare.

Author contributions

Mantu Hudait: Conceptualization, resources, supervision, project administration, funding acquisition, methodology, data curation, investigation, visualization, writing original draft, reviewing and editing; Steven Johnston: Resources, lifetime data collection, investigation, writing – review and editing; Michael Clavel: Investigation, methodology, measurement, writing – review and editing; Shuvodip Bhattacharya: measurement, analysis, editing; Sengunthar Karthikeyan:

10 | *J. Mater. Chem. C*, 2022, **00**, 1-13

This journal is © The Royal Society of Chemistry 2022

data analysis, review and editing; Rutwik Joshi: measurement, data analysis, review and editing.

Author information

Corresponding Author

*Tel: (540) 231-6663. Fax: (540) 231-3362. E-mail:

mantu.hudait@vt.edu.

ORCID

Mantu K. Hudait: 0000-0002-9789-3081

Michael B. Clavel: 0000-0002-2925-6099

This journal is © The Royal Society of Chemistry 2022

J. Mater. Chem. C, 2022, **00**, 1-13 | **11**

Notes and references

1   K. Wada and L. C. Kimerling (Editors), "*Photonics and Electronics with Germanium*", Wiley-VCH, 2015.

2   A. Elbaz, D. Buca, N. von den Driesch, K. Pantzas, G. Patriarche, N. Zerounian, E. Herth, X. Checoury, S. Sauvage, I. Sagnes, A. Foti, R. Ossikovski, J. –M. Hartmann, F. Boeuf, Z. Ikonic, P. Boucaud, D. Grützmacher and M. El Kurdi, *Nat. Photonics,* 2020, **14**, 375-382.

3   R. A. Soref, D. Buca, and S. –Q. Yu, *Opt. Photon. News* 2016, **27**, 32-39.

4   D. Stange, S. Wirths, R. Geiger, C. Schulte-Braucks, B. Marzban, N. von den Driesch, G. Mussler, T. Zabel, T. Stoica, J. –M. Hartmann, S. Mantl, Z. Ikonic, D. Grützmacher, H. Sigg, J. Witzens and D. Buca, *ACS Photonics,* 2016, **3**, 1279-1285.

5   Y. Zhou, W. Dou, W. Du, S. Ojo, H. Tran, S. A. Ghetmiri, J. Liu, G. Sun, R. Soref, J. Margetis, J. Tolle, B. Li, Z. Chen, M. Mortazavi and S. –Q. Yu, *ACS Photonics,* 2019, **6**, 1434-1441.

6   S. Assali, A. Dijkstra, A. Attiaoui, E. Bouthillier, J. E. M. Haverkort and O. Moutanabbir, *Phys. Rev. Appl.,* 2021, **15**, 024031.

7   S. Assali, A. Dijkstra, A. Attiaoui, E. Bouthillier, J. E. M. Haverkort and O. Moutanabbir, *Appl. Phys. Lett.,* 2021, **118**, 110502.

8   B. Marzban, D. Stange, D. Rainko, Z. Ikonic, D. Buca, and J. Witzens, *Photon. Res.* 2021, **9**, 1234.

9   N. Margalit, C. Xiang, S. M. Bowers, A. Bjorlin, R. Blum and J. E. Bowers, *Appl. Phys. Lett.,* 2021, **118**, 220501.

10 C. Shang, Y. Wan, J. Selvidge, E. Hughes, R. Herrick, K. Mukherjee, J. Duan, F. Grillot, W. W. Chow and J. E. Bowers, *ACS Photonics,* 2021, **8**, 2555-2566.

11 H. Tran, T. Pham, J. Margetis, Y. Zhou, W. Dou, P. C. Grant, J. M. Grant, S. Al-Kabi, G. Sun, R. A. Soref, J. Tolle, Y. –H. Zhang, W. Du, B. Li, M. Mortazavi and S. –Q. Yu, *ACS Photonics,* 2019, **6**, 2807-2815.

12 G. –E. Chang, S. –Q. Yu, J. Liu, H. –H. Cheng, R. A. Soref and G. Sun, *IEEE J. Sel. Topics Quantum Electron.,* 2022, **28**, 3800611.

13 S. Saito, A. Z. Al-Attili, K. Oda and Y. Ishikawa, *Semicond. Sci. Technol.*, 2016, **31**, 043002.

14 S. Saito, F. Y. Gardes, A. Z. Al-Attili, K. Tani, K. Oda, Y. Suwa, T. Ido, Y. Ishikawa, S. Kako, S. Iwamoto and Y. Arakawa, *Frontiers Mater*., 2014, **1**, 1.

15 C. Xu, D. Ringwala, D. Wang, L. Liu, C. D. Poweleit, S. L. Y. Chang, H. L. Zhuang, J. Menendez and J. Kouvetakis, *Chem. Mater.,* 2019, **31**, 9831-9842.

16 L. Wang, Y. Zhang, Y. Wu, T. Liu, Y. Miao, L. Meng, Z. Jiang and H. Hu, *IEEE Trans. Electron. Devices,* 2020, **67**, 3229-3234.

17 S. Wirths, R. Geiger, N. von den Driesch, G. Mussler, T. Stoica, S. Mantl, Z. Ikonic, M. Luysberg, S. Chiussi, J. M. Hartmann, H. Sigg, J. Faist, D. Buca and D. Grützmacher, *Nat. Photonics,* 2015, **9**, 88-92.

18 S. Gupta, B. Magyari-Köpe, Y. Nishi and K. C. Saraswat, *J. Appl. Phys.,* 2013, **113**, 073707.

19 D. Saladukha, M. B. Clavel, F. Murphy-Armando, G. Greene-Diniz, M. Gruening, M. K. Hudait and T. J. Ochalski, *Phys. Rev. B,* 2018, **97**, 195304.

20 M. Clavel, D. Saladukha, P. Goley, T. J. Ochalski, F. Murphy-Armando, R. J. Bodnar, and M. K. Hudait, *ACS Appl. Mater. Inter.,* 2015, **7**, 26470-26481.

21 M. K. Hudait, M. B. Clavel, L. Lester, D. Saladukha, T. J. Ochalski, and F. Murphy-Armando, *Proc. SPIE **9755**, Quantum Sensing and Nano Electronics and Photonics XIII, 97550Y* (February 13, 2016).

22 S. Wirths, A. T. Tiedemann, Z. Ikonic, P. Harrison, B. Holländer, T. Stoica, G. Mussler, M. Myronov, J. M. Hartmann, D. Grützmacher, D. Buca and S. Mantl, A*ppl. Phys. Lett.,* 2013, **102**, 192103.

23 J. –S. Liu, M. B. Clavel and M. K. Hudait, *IEEE Trans. Electron Dev.*, 2015, **62**, 3223-3228.

24 J. –S. Liu, M. B. Clavel and M. K. Hudait, *IEEE Trans. Electron Dev.*, 2017, **64**, 2193-2200.

25 Y. Zhu, D. Maurya, S. Priya and M. K. Hudait, *ACS Appl. Mater. Inter.,* 2014, **6**, 4947-4953.

26 M. Clavel, P. S. Goley, N. Jain, Y. Zhu, and M. K. Hudait, *IEEE J. Elec. Dev. Soc.* 2015, **3**, 184-193.

27 Y. Kim, S. Assali, D. Burt, Y. Jung, H. –J. Joo, M. Chen, Z. Ikonic, O. Moutanabbir and D. Nam, *Adv. Optical Mater.,* 2021, **10**, 2101213.

28 M. Oehme, K. Kostecki, K. Ye, S. Bechler, K. Ulbricht, M. Schmid, M. Kaschel, M. Gollhofer, R. Körner, W. Zhang, E. Kasper and J. Schulze, *Opt. Express,* 2014, **22**, 839-846.

29 B. R. Conley, A. Mosleh, S. A. Ghetmiri, W. Du, R. A. Soref, G. Sun, J. Margetis, J. Tolle, H. A. Naseem and S. –Q. Yu, *Opt. Express,* 2014, **22**, 15639-15652.

30 B. R. Conley, J. Margetis, W. Du, H. Tran, A. Mosleh, S. A. Ghetmiri, J. Tolle, G. Sun, R. Soref, B. Li, H. A. Naseem and S. –Q. Yu, *Appl. Phys. Lett.,* 2014, **105**, 221117.

31 T. Pham, W. Du, H. Tran, J. Margetic, J. Tolle, G. Sun, R. A. Soref, H. A. Naseem, B. Li and S. –Q. Yu, *Opt. Express,* 2016, **24**, 4519-4531.

32 E. Kasper, M. Kittler, M. Oehme and T. Arguirov, *Photon. Res.,* 2013, **1**, 69-76.

33 H. Lin, Z. Luo, T. Gu, L. C. Kimerling, K. Wada, A. Agarwal and J. Hu, *Nanophotonics,* 2017, **7**, 393-420.

34 J. F. Liu, X. Sun, D. Pan, X. X. Wang, L. C. Kimerling, T. L. Koch and J. Michel, *Opt. Express,* 2007, **15**, 11272-11277.

35 B. R. Dutt, D. S. Sukhdeo, D. Nam, B. M. Vulovic, Z. Yuan and K. C. Saraswat, *IEEE J. Photonics,* 2012, **4**, 2002-2009.

36 D. Liang and J. E. Bowers, *Nat. Photonics,* 2010, **4**, 511-517.

37 M. Seifried, G. Villares, Y. Baumgartner, H. Hahn, M. Halter, F. Horst, D. Caimi, C. Caer, M. Sousa, R. F. Dangel, L. Czornomaz and B. J. Offrein, *IEEE J. Sel. Top. Quantum Electron.,* 2018, **24**, 1-9.

38 N. von den Driesch, D. Stange, D. Rainko, I. Povstugar, P. Zaumseil, G. Capellini, T. Schröder, T., Denneulin, Z. Ikonic, J. –M. Hartmann, H. Sigg, S. Mantl, D. Grützmacher and D. Buca, *Adv. Sci.* 2018, **5**, 1700955.

39 J. Wang and S. Lee, *Sensors,* 2011, **11**, 696-718.

40 B. Julsgaard, N. V. D. Driesch, P. Tidemand-Lichtenberg, C. Pedersen, Z. Ikonic and D. Buca, *Photonics Research,* 2020, **8**, 788-798.

41 E. Vitiello, S. Rossi, C. A. Broderick, G. Gravina, A. Balocchi, X. Marie, E. P. O'Reilly, M. Myronov and F. Pezzoli, *Phys. Rev. Appl.,* 2020, **14**, 064068.

42 J. J. Sheng, D. Leonhardt, S. M. Han, S. W. Johnston, J. G. Cederberg and M. S. Carroll, *J. Vac. Sci. Technol.* B, 2013, **31**, 051201.

43 E. Rogowicz, J. Kopaczek, J. Kutrowska-Girzycka, M. Myronov, R. Kudrawiec and M. Syperek, *ACS Appl. Electron. Mater.,* 2021, **3**, 344-352.

44 E. Gaubas, J. Vanhellemont, E. Simoen, I. Romandic, W. Geens and P. Clauws, *Phys. B Condens. Matter*, 2007, **401–402**, 222-225.

45 J. Allerbeck, A. J. Herbst, Y. Yamamoto, G. Capellini, M. Virgilio and D. Brida, *Appl. Phys. Lett.,* 2019, **114**, 241104.

46 D. S. Sukhdeo, S. Gupta, K. C. Saraswat, D. Dutt and D. Nam, *Opt. Commun.,* 2016**, 364**, 233-237.

47 R. Geiger, J. Frigerio, M. J. Süess, D. Chrastina, G. Isella, R. Spolenak, J. Faist and H. Sigg, *Appl. Phys. Lett.*, 2014, **104**, 062106.

48 D. Nam, J. –H. Kang, M. L. Brongersma and K. C. Saraswat, *Opt. Lett.*, 2014, **39**, 6205-6208.

49 E. Vitiello, S. Rossi, C. A. Broderick, G. Gravina, A. Balocchi, X. Marie, E. P. O'Reilly, M. Myronov and F. Pezzoli, *Phys. Rev. Appl.,* 2020, **14**, 064068.

50 M. Bertrand, Q. –M. Thai, J. Chretien, N. Pauc, J. Aubin, L. Milord, A. Gassenq, J. –M. Hartmann, A. Chelnokov, V. Calvo and V. Reboud, *Ann. Phys.* (*Berlin*), 2019, **531**, 1800396.

51 S. Sant and A. Schenk, *Appl. Phys. Lett.,* 2014, **105**, 162101.

52 M. B. Clavel, G. Green-Diniz, M. Gruning, K. T. Henry, M. Kuhn, R. J. Bodnar, and M. K. Hudait, *ACS Appl. Electro. Mater.,* 2019, **1**, 2646 - 2654.

53 S. Johnston, R. Ahrenkiel, P. Dippo, M. Page and W. Metzger, *Mater. Res. Soc. Symp. Proc*., 2007, **994**, 0994-F07-04.

54 S. Johnston, K. Zaunbrecher, R. Ahrenkiel, D. Kuciauskas, D. Albin and W. Metzger, *IEEE. J. Photovolt.*, 2014, **4**, 1295-1300.

55 M. B. Clavel, J. -S. Liu, M. A. Meeker, G. A. Khodaparast, Y. Xie, J. J. Heremans, S. Bhattacharya and M. K. Hudait, *J. Appl. Phys.* 2020, **127**, 075702.

56 M. B. Clavel, J. -S. Liu and M. K. Hudait, *ACS Omega,* 2022, **7**, 5946-5953.

57 J. -M. Chauveau, Y. Androussi, A. Lefebvre, J. Di Persio, and Y. Cordier, *J. Appl. Phys.,* 2003, **93**, 4219.

58 M. K. Hudait, Y. Zhu, N. Jain and J. L. Hunter Jr., *J. Vac. Sci. Technol.* B, 2013, **31**, 011206.

59 R. Roucka, J. Xie, J. Kouvetakis, J. Mathews, V. D'Costa, J. Menendez, J. Tolle and S. –Q. Yu, *J. Vac. Sci. Technol.* B, 2008, **26**, 1952.

60 J. Xie, J. Tolle, V. D'Costa, C. Weng, A. V. G. Chizmeshya, J. Menendez and J. Kouvetakis, *Solid-State Electron*., 2009, **53**, 816-823.

61 P. Ščajev, V. Soriūtė, G. Kreiza, T. Malinauskas, S. Stanionytė, P. Onufrijevs, A. Medvids and H. –H. Cheng, *J. Appl. Phys.,* 2020, **128**, 112101.

62 E. Gaubas and J. Vanhellemont, *Appl. Phys. Lett.,* 2006, **89**, 142106.

63 Dieter K. *Schroder*, "*Semiconductor Material and Device Characterization*", pp. 389-464, 3rd Edition, Wiley, Year 2005.

64 X. Li, A. C. Walhof, W. Dai, I. Arslan, Y. Liu, F. Toor, and J. P. Prineas, *Opt. Mater. Express* 2021, **11**, 719-728.

65 N. Jain and M. K. Hudait, *IEEE J. Photovoltaics* 2013, **3**, 528.